Thermodynamic characterization of amyloid polymorphism by Taylor dispersion analysis

Azad Farzadfard[1,2], Antonin Kunka[1], Thomas Oliver Mason[1], Jacob Aunstrup Larsen[1], Rasmus Krogh Norrild[1], Elisa Torrescasana Dominguez[1], Soumik Ray[1], and Alexander K. Buell[1]*,

1- Protein Biophysics group, Department of Biotechnology and Biomedicine, Technical University of Denmark, Søltofts Plads, Building 227, 2800, Kgs. Lyngby, Denmark

2- Interdisciplinary Nanoscience Center (iNANO), Aarhus University, Gustav Wieds Vej 14, 8000, Aarhus C, Denmark

Abstract:

Amyloid fibrils of proteins such as α-synuclein are a hallmark of neurodegenerative diseases and much research has focused on their kinetics and mechanisms of formation. The question as to the thermodynamic stability of such structures has received much less attention. Here, we present a novel experimental method to quantify amyloid fibril stability based on chemical depolymerisation and Taylor dispersion analysis. The relative concentrations of fibrils and monomer at equilibrium are determined through an in situ separation of these species through Taylor dispersion in laminar flow inside a microfluidic capillary. This method is highly sample economical, using much less than a microliter of sample per data point and its only requirement is the presence of aromatic residues because of its label-free nature. Using this method, we investigate the differences in thermodynamic stability between different fibril polymorphs of α-synuclein and quantify these differences for the first time. Importantly, we show that fibril formation can be under kinetic or thermodynamic control and that a change in solution conditions can both stabilise and destabilise amyloid fibrils. Taken together, our results establish the thermodynamic stability as a well-defined and key parameter that can contribute towards a better understanding of the physiological roles of amyloid fibril polymorphism.

Introduction:

Amyloid fibrils are a specific class of protein aggregates characterized by a highly ordered, elongated molecular architecture formed by repeating intermolecular β-sheet motifs. Their accumulation in intra- or extracellular deposits is a common denominator of numerous severe pathologies including Alzheimer's disease (AD), Parkinson's disease (PD), or Amyotrophic lateral sclerosis (ALS) [1]. The individual building blocks of amyloid fibrils are structurally distinct from their soluble precursors which range from short peptides [2], intrinsically disordered proteins (IDPs [3]), to natively folded proteins [4-7], indicating a certain universality of the "amyloid fold" [8]. Conversely, cryo-electron microscopy of several amyloid-forming proteins revealed a high degree of structural polymorphism, i.e., a single

polypeptide chain adopting several distinct conformations within the amyloid core [9-11]. Fibril polymorphism is strongly modulated by extrinsic factors and consequently, structures of fibrils formed *in vitro* often do not correspond to those isolated *ex vivo* from patients' tissues [11]. Moreover, several polymorphs have been identified in a single test tube in which initially highly pure soluble protein (α-Synuclein) aggregated under well-defined solution conditions [12]. Altogether, it is now increasingly more apparent that the free-energy landscape of amyloids is much more degenerate than perhaps originally thought, and that fibril polymorphism is a consequence of the interplay between kinetic factors and stability of individual conformations.

The thermodynamic stability of amyloids fibrils can provide the missing link for understanding the mechanisms driving fibril polymorphism. In contrast to the kinetics of amyloid formation which has been extensively studied [13-15] and characterized in detail for many pathologically relevant proteins such as Amyloid-β [16], Tau [17], or α-Synuclein (αSyn) [18-19], systematic analysis of amyloid stability has only recently started to gain more attention [20]. The thermodynamic stability of amyloid fibrils may contribute to defining their persistence *in vivo*, which is influenced by many factors including posttranslational modifications [21-22], proteasomal degradation [23], or clearance by chaperones [24-26]. The dysregulation and insufficient efficiency of these clearance mechanisms leads to pathological states.

In general, thermodynamic stability is defined by the concentration of different species in equilibrium, e.g., folded, and unfolded states for protein conformational stability (Equation 1). Similarly, the thermodynamic stability of amyloid fibrils can be defined by the concentration of soluble precursors (herein termed monomers) in equilibrium with the insoluble fibrils. At sufficiently high total concentration, the equilibrium concentration of monomer is independent of the molar concentration of fibrils and relates to fibril stability according to Equation 2.

Eq. 1 $U \rightleftharpoons N$; then $\Delta G_0 = -RT\, ln\left([N]_{eq}/[U]_{eq}\right)$

Eq.2 $[F]_n + [M] \rightleftharpoons [F]_{n+1}$; then $\Delta G_0 = -RT\, ln\left(1/[M]_{eq}\right)$;

where R is the universal gas constant, T is absolute temperature (K), and [F] and [M] are protein concentrations in fibrillar (insoluble) and monomeric (i.e., soluble) states, respectively [20]. The amyloid state is thought to be the global energy minimum of the protein free energy landscape. Consequently, high thermodynamic stability of fibrils translates to low concentrations of soluble protein at the end of the aggregation reaction which are often difficult to quantify accurately [27-28]. In order to increase the equilibrium concentration of soluble protein to easily quantifiable levels, the equilibrium can be shifted in favour of fibril dissociation by changing external conditions, e.g., increasing (or decreasing) temperature [29-33], high pressure [34], or by addition of chemical denaturants [35-38]. The latter is perhaps the most versatile since, similarly to protein unfolding, a linear dependence of Gibbs free energy on denaturant concentration can be reasonably assumed [35, 39] which allows for the application of a

(relatively) straightforward analytical framework. This typically involves fitting chemical depolymerization data to an isodesmic polymerisation model, in which a single equilibrium constant is assumed between monomers and aggregates regardless of their size [40-41]. Recently, a more realistic cooperative model has been applied to the analysis of depolymerization of glucagon and PI3K-SH3 domain fibrils [38].The model recognizes nucleation and polymerization through two distinct equilibrium constants and is able to correctly model the protein concentration dependency of the depolymerization curves [38].

Chemical depolymerization offers several advantages including simplicity and scalability. Experimental techniques used in chemical depolymerization experiments can be categorized into two groups: (i) separation-based, and (ii) bulk methods. The first group relies on physical separation of the soluble protein from the fibrils, and their subsequent quantification. Methods including (ultra) centrifugation [41] or chromatography (HPLC) are often used, although they are time and sample consuming. Techniques from the second group rely on monitoring changes in specific features of fibrils or monomers as a function of increasing denaturant concentration, and include, for example, circular dichroism, light scattering, intrinsic fluorescence, or Thioflavin-T fluorescence [35]. Spectroscopic techniques have the advantage of analyzing mixtures without the need for separation, which enables fast and high-throughput analysis. However, these methods provide relative measurements rather than absolute concentrations of the species involved which introduces some degree of uncertainty during analysis. Furthermore, they might require presence of specific fluorophores (intrinsic fluorescence) and can be limited by strong scattering (circular dichroism).

Here, we present a novel approach for the analysis of fibril stability by chemical depolymerization which combines the advantages of both categories. Our method utilizes flow-induced dispersion analysis (FIDA) for separation of monomers from fibrils and quantification of monomer concentration within a thin fused-silica capillary. The approach is rapid, fully automated, amenable to high throughput, label-free, utilizes a commercially available instrument, and uses minute amounts of sample. We demonstrate its advantages by benchmarking it against four commonly used techniques using αSyn and PI3K-SH3 fibrils as the test cases. Using our newly developed approach we compare stability of fibrils at different experimental conditions and quantify thermodynamic stability differences between distinct fibril polymorphs. We believe that our new method is a versatile and useful tool for probing rugged amyloid landscapes in a quantitative, and efficient manner.

Results

Flow-induced dispersion analysis of non-diffusive particles

In this study, we employ flow-induced dispersion analysis (FIDA) to measure the thermodynamic stability of αSyn and PI3K-SH3 fibrils. FIDA utilizes Taylor dispersion [42] to measure the size of the particles based on their diffusivity in a laminar flow defined by low values of the Reynolds number (Re < 2000; typical scenarios in FIDA experiments feature 0.1 > Re > 10 in water and 25 °C). In the laminar flow regime, the fluid travels in parallel layers that move smoothly next to each other without turbulent mixing. The central layers are the fastest while the outermost layers in contact with the capillary wall are immobile, giving rise to the characteristic parabolic flow velocity profile. Consequently, the mass transfer between these fluid layers in the directions perpendicular to the flow can only be achieved by radial diffusion (see **supplementary movie**). Small particles (e.g., small molecules, proteins) diffuse between the layers and travel with the average flow velocity (**Figure 1 a**, and supplementary movie, blue species) resulting in a Gaussian distribution of their concentration at the point of the detection. Their diffusion coefficients (D_{app}) can be obtained by fitting the resulting Taylorgrams by equations (Eq. 3 and 4) and used to determine their hydrodynamic radii (R_h) according to the Stokes-Einstein equation (Eq. 5) [43-44].

Eq. 3 $$y = y_0 + \frac{A}{2\sigma\sqrt{\pi/2}} e^{\left(-\frac{(t-t_R)^2}{2\sigma^2}\right)}.$$

Eq.4 $$D_{app} = t_R a^2/24\sigma^2$$

Eq. 5 $$R_h = \frac{k_B.T}{6\pi.\eta.D_{app}}$$

where σ^2 and t_R are variance and residence time of the peak, respectively, and a is the inner diameter of the capillary.

Conversely, larger particles ($R_h \gtrapprox 100$ nm; e.g., liposomes, large nanoparticles, protein aggregates) cannot radially diffuse (or diffuse marginally within the < 1 minute experimental time scale) and remain in the same flow layer during the experiments, resulting in the deformed, asymmetrical distribution of their signal at the detector (**Figure 1 b and c**; supplementary movie, green species).

Here, we exploit this phenomenon to separate non-diffusive aggregates from the diffusive monomers to determine the stability of amyloid fibrils. To better understand the behaviour of the diffusive and non-diffusive particles during FIDA, we first numerically simulated the experiment using the COMSOL software (COMSOL Multiphysics® v. 6.1. COMSOL AB, Stockholm, Sweden). In the simulations, a small plug (20 s, 75 mbar) containing a mixture of nanoparticles (NPs, $D = 2.5\times10^{-12}$ $m^2.s^{-1}$, corresponding to $R_h = 100$ nm) and protein monomers ($D = 7.0\times10^{-11}$ $m^2.s^{-1}$, corresponding to $R_h = 3.5$ nm derived from FIDA measurements of αSyn monomer) was injected into the one meter-long capillary

with internal diameter of 75 µm, and their time-dependent distribution in 1500 mbar flow was analyzed (**Figure 1 d and e**; Supplementary movie). Expectedly, the radially diffusing monomers formed a wide uniform zone which travels with the average flow speed (Figure 1 d and e; Supplementary movie). In contrast, the non-diffusive NPs follow the parabolic shape of the flow speed with their major fraction being pushed ahead of the plug, followed by the gradually decreasing fraction moving in the slower layers. This translates to a highly skewed distribution at the point-of-detection (84 cm from the injection) with sharp increase in signal followed by its slow gradual decrease over time (Figure 1 d and e; Supplementary movie). A COMSOL simulation of different particle sizes are shown in **SI figure 1**.

To validate our simulations, we carried out the experiment in the FIDA instrument using αSyn monomers (wt or F94W mutant) and fluorescent carboxylate-modified polystyrene NPs (d = 200 nm; FluoSpheres™, Thermo Fisher) as the models of diffusive and non-diffusive particles, respectively (Figure 1 a-c). The experimental flow profiles of the two types of species match almost perfectly those obtained by the COMSOL simulations (Figure 1 e). Moreover, the behaviour of the non-diffusive particles can be well approximated by an analytical solution derived in our previous development of Taylor dispersion-induced phase separation (TDIPS [45]). As predicted by both the simulations and the analytical equations, the arrival time of the fastest non-diffusive particles is almost exactly half of the average monomer residence time.

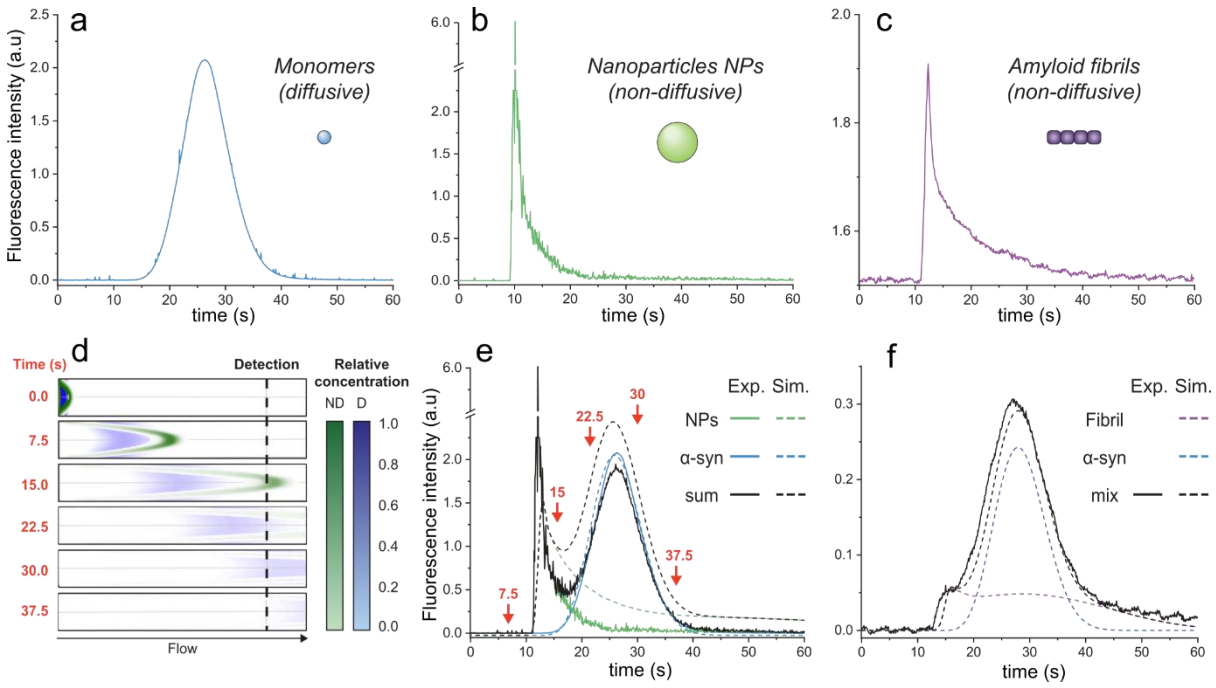

Figure 1. Flow-induced dispersion analysis (FIDA) of diffusive and non-diffusive particles. FIDA of (a) monomeric αSyn (Rh = 3.5 nm), (b) fluorescent nanoparticles (d = 200 nm), and (c) F94W αSyn amyloid fibrils (non-sonicated large fibrils). Experiments were recorded under the same experimental conditions (i.e., flow rates, volumes) described in the materials and methods. (d)-(f) COMSOL simulations of FIDA using a mixture of monomeric αSyn and nanoparticles. (d) Snapshots of the mixture separating in the capillary (i.d. = 75 µm, l = 1

m) at different time-points (See Supplementary movie for the whole simulation). Concentrations of the non-diffusive (ND) and diffusive (D) particles in the flow are indicated by the colour-gradients shown on the right. (e) Overlay of the simulated Taylorgrams shown on the left with the sum of the experimentally measured FIDA of D and ND species, corresponding to curves in (a) and (b). The arrows correspond to the time points shown as snapshots in (d). (f) Comparison of experimental (black line) and simulated (dashed lines) data for a mixture of F94W αSyn monomers (blue) and sonicated fibrils (purple; length ~ 100 nm, Rh = 20.3 nm) in 1 M urea.

Amyloid fibrils behave as non-diffusive particles during FIDA.

Following the successful modelling and experimental validation of the NPs behaviour during FIDA, we extended the methodology to the analysis of amyloid fibrils (**Figure 1 f**). We used αSyn fibrils equilibrated in 1 M urea to allow their partial dissociation to monomers and analyzed the resulting mixture using FIDA (Figure 1 f). The profile resembled the one obtained as the sum of NPs and monomeric αSyn (Figure 1 e), suggesting similar, non-diffusive behaviour of the fibrils. We analyzed the curve using numerical COMSOL simulations assuming two species and obtained diffusion coefficients of 7.0×10^{-11} and 1.2×10^{-11} $m^2.s^{-1}$ for αSyn monomer and fibril, respectively. Both values are in excellent agreement with those measured by FIDA of αSyn monomers (Rh = 3.5 nm), and DLS analysis of fibrils (Rh = 20.3 ± 0.5 nm). The latter corresponds to a fibrillar species of around 100 nm length with 10 nm width based on the models of rod-like particles derived elsewhere [46]. Together, our results clearly demonstrate that FIDA is a suitable method for separation and individual quantification of diffusive soluble proteins from their mixtures with non-diffusive particles.

Chemical depolymerization of αSyn fibrils studied using FIDA

Next, we repeated the experiment in a range of urea concentrations to derive the full depolymerization curve of the αSyn fibrils. First, we tested fibrils of the αSyn tryptophan-containing mutant (F94W) to obtain a higher signal-to-noise ratio compared to the wild type in the intrinsic fluorescence-based detection system. We analyzed F94W αSyn fibrils equilibrated in a range of urea concentrations from 0 to 5.4 M using FIDA (**Figure 2**). For each sample, a buffer with the matching concentration of urea was used as surrounding of the sample plug to avoid artifacts from dilution or viscosity gradients. In low concentrations of urea, the resulting Taylorgrams were characteristic of the two-component system described above, i.e., sum of asymmetrical and Gaussian peaks (Figure 2 b). The amplitude of the former gradually decreased and completely disappeared at high urea concentrations (> 2.28 M), indicating complete fibril dissociation. Similar to the experiments described above, the monomer diffusion in the complex mixture was mostly unaffected by the larger species and behaved in a predictable manner which could be accurately modelled and analyzed (Figure 2 c). Conversely, the signal from protein aggregates was less reproducible due to the unspecific self-interaction or interaction with the capillary surface resulting in signal spikes or delayed elution (sometimes appearing in the washing step). Therefore, we concluded that absolute quantification of monomers, rather than relative quantification of fibrils and monomer is a more robust and reproducible approach and used it for further analysis. We verified that florescence and hydrodynamic radius of the monomer are not affected by the

denaturant by performing control experiments with monomeric αSyn in increasing concentrations of urea (**SI figure 2**).

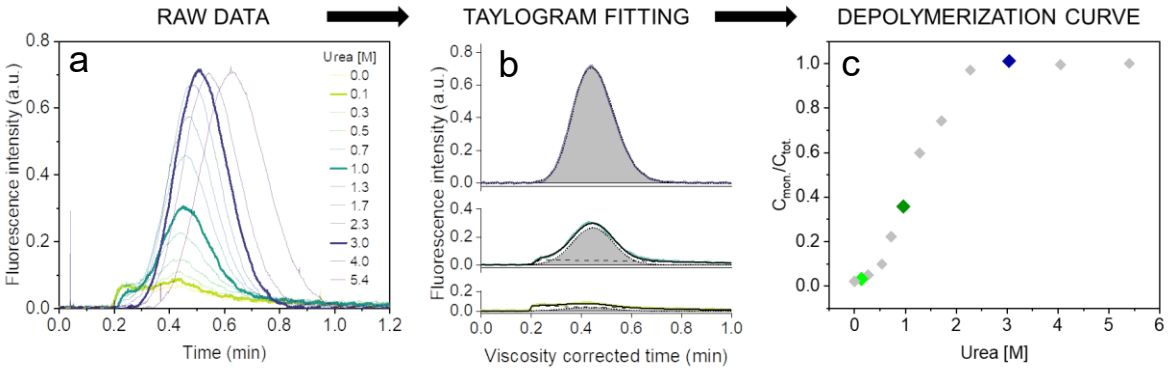

Figure 2: Chemical depolymerization of amyloid fibrils using FIDA. (a) Raw Taylorgrams of F94W fibrils (c = 20 μM) equilibrated in increasing concentrations of urea. (b) Quantification of monomer concentration from the Taylorgrams (after correction for the urea viscosity, see materials and methods). Fitting of three representative curves (highlighted in the panel (a)) by the sum of the equations describing asymmetrical (dotted line) and Gaussian (dashed lines) distributions (Eqs. 6 and 7). The area of the Gaussian peak (gray) is proportional to the monomer concentration. (c) Depolymerization curve of F94W αSyn fibrils. The points correspond to the ratio of monomer concentrations derived from the Taylorgram fitting and the total protein concentration as a function of urea.

The quantification of monomer was carried out in several different ways. First, we removed the signal contribution from the fibrils by subtracting a manually generated linear baseline connecting the hypothetical intersections of the two distinct peaks and integrated the remaining monomer peak to obtain the corresponding area (**SI figure 3**, **SI table 1**). Although simple, the procedure is lengthy and subjective regarding the selection of the intersects. To overcome these limitations, we fitted the viscosity-corrected data to the sum of the two distributions described by equations 6 and 7 (see Materials and Methods for details) to obtain the deconvoluted areas under the Gaussian peaks. The procedure worked well for curves where the two distributions could be clearly distinguished. In cases where the contribution from one of the peaks to the overall signal was minimal (0 to 10%), analysis was more challenging and often resulted in overfitting due to the high number of parameters. We solved this by writing a custom python script that globally fits the Taylorgrams across the whole urea concentration range by parametrizing the monomer peak area using ΔG and m-value from the isodesmic model and sharing the rest of the parameters from equations 6 and 7 (except the area of the asymmetric fibril peak). The global analysis gives well defined confidence intervals of the fitted parameters, albeit sometimes at the expense of quality of the individual fits. Finally, we verified the results using deconvolution of the curves by numerical analysis in COMSOL. The depolymerization curves obtained by the four methods are almost identical and yield similar energy parameters (within error) when analyzed within the isodesmic depolymerization model framework (SI figure 2). We chose the global fitting approach for analysis of further experiments owing to its reliability, speed, and automation.

FIDA is a robust method for the analysis of amyloid fibril thermodynamic stability.

To validate our newly developed FIDA analysis, we measured the thermodynamic stability of the WT and F94W mutant of αSyn, and PI3-SH3 fibrils using other available techniques including DSF (differential scanning fluorimetry), static light scattering (SLS) intensity, Thioflavin T fluorescence, and ultracentrifugation (UCF) followed by quantification of the monomer in the supernatant using UV-absorbance (**Figure 3, Table 1**). Depolymerization curves obtained by each method were fitted to the isodesmic model with shared m-value to reduce its correlation with ΔG, making the quantitative comparison of individual fits in terms of the latter parameter more reliable and straightforward. The isodesmic model is conceptually simpler than the cooperative model which limits overfitting by reducing the number of free parameters, particularly in cases where only a single protein concentration is measured [38]. We obtained excellent agreement between experiments for the F94W αSyn with nearly overlapping depolymerization curves (apart from that obtained by ThT fluorescence) and differences between ΔG values within the range of fitting errors (**Figure 3 a,** Table 1). Since both FIDA and DSF are based on the detection of intrinsic fluorescence, we decided to test their limits by repeating the experiment using fibrils of wild type αSyn which does not contain tryptophan, but only 4 tyrosine residues as fluorophores (**Figure 3 b,** Table 1). The fibrils were prepared according to the same protocol used for the F94W mutant and depolymerized at two-times higher final concentration (40 μM) to compensate for the signal loss. The sensitivity of the FIDA proved to be sufficient and we were able to obtain a well-defined depolymerization curve (Figure 3 b). In contrast, DSF which utilizes the shift of the tryptophan fluorescence emission spectrum induced by changes in its local environment (e.g., monomeric vs fibrillar state [47-48]) did not yield any meaningful results (Figure 3 b), confirming that the tyrosine residues lack the environmental sensitivity necessary to distinguish aggregated from soluble states. Interestingly, the stability of WT fibrils was ca. 5 $kJ.mol^{-1}$ lower compared to the F94W mutant (Table 1). This difference is higher than the variability of ΔG values obtained for WT using different techniques (~3 $kJ.mol^{-1}$). Arguably, the mutation alters the energy landscape of αSyn and is therefore not a non-invasive probe for analysis of αSyn fibril stability. This is an important finding since similar effects might be, in principle, observed in studies of amyloid forming proteins lacking tryptophan and that use engineered Trp variants instead.

In contrast to αSyn, the SH3 domain of phosphatidyl-inositol-3-kinase (PI3K-SH3) contains a single tryptophan which gives the protein two distinct fluorescence emission spectra in a monomeric and fibrillar state (fluorescence is fully quenched in the fibrillar state), making it an ideal probe for studying fibril stability by DSF [38]. Our analysis of PI3K-SH3 fibril stability by FIDA agreed well with DSF measured here (**Figure 3 c**, Table 1) and published previously [38]. In contrast, the SLS signal was noisy at low denaturant concentrations, presumably due to higher order assembly of fibrils and sedimentation and could not be used for the fitting.

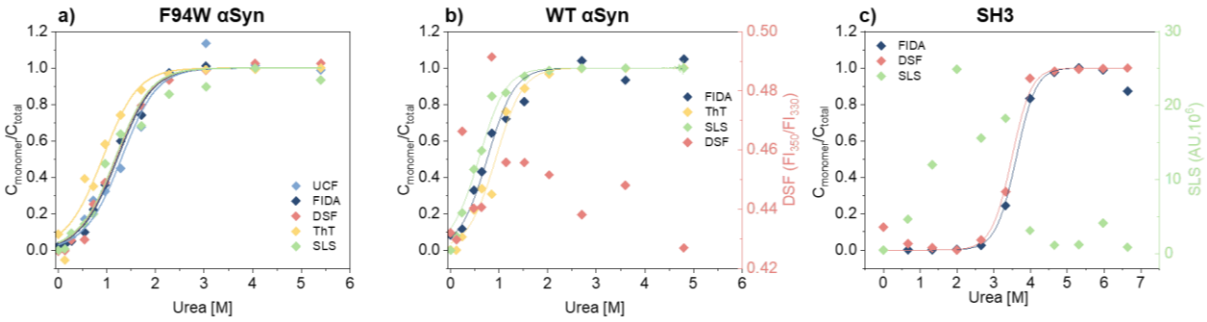

Figure 3: Thermodynamic stability of three different amyloid fibrils measured with different techniques. (a) Chemical depolymerisation of F94W αSyn mutant fibrils was studied reliably with all techniques including ultracentrifugation (UCF), FIDA, DSF, ThT and SLS. Data from ThT fluorecence is slightly out of the error range of the other techniques. (b) WT αSyn fibrils were reliably measured by FIDA, ThT and SLS, however, DSF failed to monitor the monomer/fibril conversion as expected due to lack of W amino acids. (c) PI3K-SH3 amyloid fibrils were measured reliably by FIDA and DSF, but SLS intensity data was unreliable most probably due to precipitation at low denaturant concentrations. Non-normalized data for DSF in (b) and SLS intensities in (c) are shown in the second Y axis of the corresponding graphs.

Using three model cases we successfully verified the general applicability of our novel approach for analyzing fibril stability. The only other method which could be successfully applied to all three cases was ThT fluorescence which is also simple, fast, and scalable. However, different fibrils have distinct sensitivity to ThT, and some fibril polymorphs are even "ThT-invisible" and cannot be monitored by this fluorescent dye [49-52]. Although applicable in some cases, scattering techniques (SLS and DLS) suffer from large dependency of scattered light intensity on aggregate size, hindering reliable normalization of the depolymerization curves when small amounts of residual aggregates are present in the depolymerized samples at high urea concentrations. Similar issues apply to ultracentrifugation, which additionally requires higher volumes of sample (> 30 µL), specialized equipment, and long centrifugation times (> 1.5 h) at high-speed (> 150,000 x g) to ensure complete removal of the aggregates.

Table 1. Comparison of thermodynamic stability of three model amyloid systems measured using different techniques.

Analytical technique	WT αSyn		F94W αSyn		SH3	
	ΔG (kJ.mol^{-1})	m (kJ.M^{-1}.mol^{-1})	ΔG (kJ.mol^{-1})	m (kJ.M^{-1}.mol^{-1})	ΔG (kJ.mol^{-1})	m (kJ.M^{-1}.mol^{-1})
UCF	n.m.		35.0 ± 0.6		n.m.	
FIDA	-31.2 ± 0.3		34.4 ± 0.6		-59.8 ± 3.5	
DSF	n.d.	9.8 ± 0.1	34.1 ± 0.6	7.4 ± 0.4	-58.6 ± 3.3	10.0 ± 1.0
ThT	-32.0 ± 0.4		32.1 ± 0.5		n.m.	
SLS	-29.5 ± 0.1		34.0 ± 0.5		n.d.	

UCF – ultracentrifugation, FIDA – Flow-induced dispersion analysis, ThT – Thioflavin T assay, SLS – static light scattering, DSF – Differential scanning fluorimetry, n.m. – not measured, n.d. – ΔG could not be determined.

Thermodynamic stability as potential indicator of aSyn fibril polymorphism

Finally, we applied our newly developed methodology to study how the solution conditions dictate the stability of WT αSyn fibrils (**Table 2**). First, we selected two well characterized αSyn fibril polymorphs – fibrils (polymorph S) assembled under physiological conditions (50 mM Tris-HCl, pH 7.4, 150 mM KCl; i.e., salt condition), and ribbons (polymorph NS) assembled in the absence of salt (5 mM Tris-HCl pH 7.4, i.e., no salt condition) [53]. We prepared the two fibril polymorphs using the established protocols [53] and confirmed their morphology using AFM (**Figure 4 c**). Fibrils of polymorph S are composed of two protofilaments (8.23 ± 1.17 nm height) that twist with an average pitch length of 204 ± 63 nm. In contrast, the ribbons were thinner (6.59 ± 0.87 nm height), had no detectable twist, and were often found in bundles (Figure 4 c). Both polymorphs were sonicated and depolymerized using increasing concentrations of urea in (i) their original buffer (native conditions) and in (ii) buffer with salt to allow direct comparison of their stability. Interestingly, although the two polymorphs showed similar stability in their native buffers, polymorph NS was 6 $kJ.mol^{-1}$ more stable than polymorph S when measured in the presence of salt (**Figure 4 a**). Using ssNMR, it has been shown that polymorph NS is formed by regular long β-strands whereas polymorph S has an irregular pattern of shorter β-strands [54]. The higher stability of polymorph NS observed here can thus arguably reflect the stronger network of hydrogen bonds within its cross-β-sheet architecture and/or higher number of residues forming the amyloid core.

Next, we studied the effect of pH on fibril stability. We prepared αSyn fibrils at pH 7.4 (neutral (N) polymorph) and 5.5 (acidic (H) polymorph) in the presence of 150 mM NaCl to mimic cytosolic and lysosomal pH, respectively [55]. We characterized their morphology using AFM and found that the neutral polymorph has an average pitch length of 162 ± 47 nm and height of 5.2 ± 0.7 (Figure 4 c). The morphology of acidic polymorph was difficult to assess due to the clumping of individual fibrils into amorphous-like large particles observed by AFM (Figure 4 c**)**. When depolymerized in their native conditions, the acidic polymorph was more stable compared to the neutral polymorph (**Figure 4 b**). However, its stability decreased significantly when transferred to the neutral condition, to below the stability of the neutral polymorph (Figure 4 b**,** Table 2**)**. Arguably, this shift of fibril stability is caused by the higher solubility of αSyn in the neutral pH compared to the acidic one leading to (partial) fibril dissociation upon the pH jump. Similar destabilization of αSyn fibrils upon change in pH was observed by others and could be an important phenomenon occurring in vivo [55].

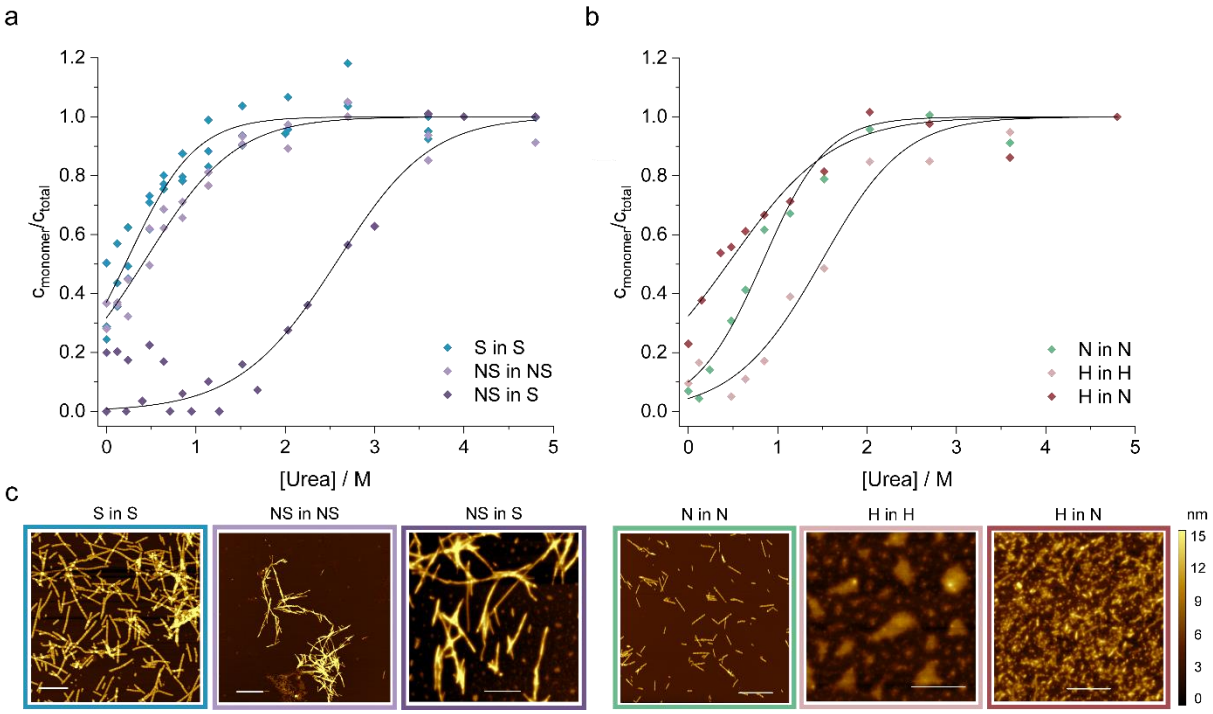

Figure 4: Chemical depolymerization of different αSyn fibrils measured under various solution conditions. (a) Stability of fibrils prepared and measured in the absence (NS, violet), or presence (S, blue) of salt. The depolymerization of the ribbons in the presence of salt (dark violet) was carried out to directly compare their stabilities. All curves were fitted to the isodesmic model of fibril depolymerization (black lines). (b) Stability of fibrils prepared and measured in neutral (pH 7.4, N, green), or acidic (pH 5, H, salmon) pH. The depolymerization of the H polymorph in neutral pH (red) was carried out to directly compare its stability with that of fibrils formed at neutral pH. All curves were fitted to the isodesmic model of fibril depolymerization (black lines). (c) AFM analysis of fibril morphologies. The H polymorph formed amorphous-like assemblies on the mica preventing reliable analysis of the individual particles.

Table 2: Thermodynamic stabilities of different WT αSyn fibril polymorphs prepared and measured under different sets of solution conditions. The Gibbs free energy difference between monomeric and fibrillar state (ΔG) and m-values were obtained from fitting the chemical depolymerization data shown in Figure 4 by the isodesmic model of depolymerization (black lines, Figure 4). The name of the polymorphs corresponds to the condition at which they were formed and is described in the buffer column (S-salt condition, NS – no salt condition, N – neutral, H – acidic).

Fibril polymorph	Condition	ΔG ($kj.mol^{-1}$)	m-value ($kJ.M^{-1}.mol^{-1}$)	Buffer
S	S	-25.2 ± 1.5	5.8 ± 1.6	50 mM Tris, 150 mM KCl pH 7.5
NS		-37.3 ± 5.3	4.5 ± 1.3	
NS	NS	-25.8 ± 0.3	5.7 ± 0.1	5 mM Tris pH 7.5
N	N	-29.9 ± 0.8	7.4 ± 0.8	20 mM NaP, 150 mM NaCl pH 7.4
H		-25.8 ± 0.5	4.6 ± 0.8	
H	H	-32.2 ± 1.0	5.7 ± 0.6	20 mM NaAc, 150 mM NaCl pH 5

Discussion:

FIDA is a robust, sensitive, and sample-economical method for analysis of fibril stability.

Several different experimental methods are used to probe thermodynamic stability of amyloid fibrils (**Table 3**) [35, 38, 41]. These include methods based on separation of the two species from each other (e.g., ultracentrifugation), or those detecting the spectroscopic or scattering signatures from mixtures of fibrils and soluble protein (e.g., ThT, DSF, SLS). Ultracentrifugation, followed by quantification of soluble protein in the supernatant, is considered a standard method for the quantification of the solubility at any given set of conditions. Despite being conceptually simple and straightforward, it is time-consuming and has relatively low throughput. Furthermore, in our study, we failed to separate extensively sonicated fibrils from monomer even by centrifugation at 180,000 x g for 1 hour. The resulting supernatant was ThT positive, indicating presence of residual fibrils or oligomers (**SI figure 4**).

Higher-order assemblies and aggregates of proteins strongly scatter light which can be used for determination of fibril stability [56-57]. The analysis of stability curves determined by DLS or SLS can be cumbersome due to the large uncertainty in quantification of soluble monomers in samples with small amounts of large aggregates that dominate the scattering signal which consequently hinders correct normalization of the depolymerization curves. Moreover, aggregates that precipitate out of solution do not show any scattering signal (e.g. SH3 fibrils, Figure 3c). The Thioflavin-T (ThT) assay is an extensively used and popular method for quantification of fibrils, mostly in kinetic analysis of fibril formation, owing to its simplicity, throughput, and use of commonly available fluorescence plate readers. One of the main disadvantages of ThT-based (or other fluorescent probes such as ANS) detection is the great sensitivity of the fluorescence intensity of the dye towards solution conditions or structural features of the fibrils [49-52, 58]. DSF is an attractive method due to its high throughput and low sample consumption. However, it requires the presence of tryptophan residues localized such that their structural context within the protein changes between monomeric and fibrillar states and is accompanied by sufficiently large shift of its fluorescence spectrum [38]. Unfortunately, tryptophan is a relatively rare amino acid [59-60] and its introduction into the wild type by mutagenesis can affect the protein's free energy landscape, as demonstrated here in a case of αSyn (Figure 3 a and b). The output of spectroscopic and scattering techniques reports only on relative concentrations of the species and the resulting data analysis requires making assumptions which might be incorrect. Specifically, the normalization of data may suffer from errors if the fibrils are partially dissociated in the absence of urea or not completely depolymerized in the highest urea concentration, where the relative monomer concentration is normalized to zero and one.

In contrast, the methodology described here combines fast, *in situ* separation of the two species using ultra-low sample volume (5 μL minimal sample volume with only a few nL sample consumption per data point) on relatively short time scales (minutes) in an automated, high throughput-amenable manner.

The intrinsic fluorescence detector is sensitive enough to detect species of protein that do not contain tryptophan. Here, down to 5 μM of monomeric unlabelled WT αSyn (ε_{280} = 5,960 $M^{-1}cm^{-1}$; four tyrosine residues) could be detected. The quantification of monomer concentration enables straightforward and reliable data normalization. Moreover, absolute concentration of monomer can be obtained if it can be independently demonstrated that the samples are fully monomeric at the highest denaturant concentrations. Otherwise, a calibration curve with known monomer concentrations can be used. Although not considered in detail in our present analysis, the fluorescence signal of the fibrils during FIDA provides valuable qualitative information about their properties. Fibrils that are prone to self-association form larger aggregates that are detected as signal spikes whose intensity is related to their size. Conversely, isolated, and homogenized (sonicated) fibrils are often small enough to appear as continuous signal of non-diffusive particles (Figure 1 c). Such information can be useful in attempts to optimize solution conditions towards favouring well-defined individual fibrils, something that is a requirement for structural analyses of amyloid fibrils, e.g. by AFM or cryoEM.

Table 3*:* Comparison of different experimental methods used for chemical depolymerization experiments.

Technique	Detection/ Species	Advantages	Disadvantages
FIDA	Intrinsic fluorescence/ monomer	Quantification of monomer, sizing of the soluble species, 5 μL/sample (>95% recoverable [a]), 15 samples/hour [b] in autonomous manner from 96 well-plate, qualitative information about fibril size[c], can be used in tandem with centrifugation [d], label-free	Requires presence of at least one Y/W in the sequence, parallel measurements not possible.
UCF	Absorbance/ monomer	Quantification of monomer, medium throughput (72 samples per run[e]), sensitivity dependent on the protein quantification assay and can be optimized.	Labor-intensive [f], large sample volume (~ 30 μL), no sizing of soluble species available, presence of soluble aggregates in the supernatant.
ThT	Extrinsic Fluorescence/ Fibril	High throughput (768 samples/hour [g]), low sample consumption (15 μL), autonomous, continuous monitoring of multiple samples during equilibration possible (depolymerization kinetics)	Low or no sensitivity to certain fibrils (i.e., ThT invisible polymorphs), indirect measurement [h], interference with other molecules (e.g., DNA), no information about the soluble species which can render normalization difficult.

SLS, DLS	Light scattering/ Fibrils	Simple and fast, high throughput (48 samples/run [i]), low sample consumption (10 µL [i]). label-free, no specific protein amino acid requirements, continuous monitoring of multiple samples during equilibration possible (depolymerization kinetics)	Large dependence of scattering intensity on aggregate size, no information about the concentration of the soluble species leading to errors in data normalization, low signal/noise ratio.
DSF	Intrinsic fluorescence/ both	Simple and fast, high throughput (48 samples/run [i]), low sample consumption (10 µL [i]), continuous monitoring of multiple samples during equilibration possible (depolymerization kinetics).	Requires presence of tryptophan residues and measurable difference of their fluorescence spectra in the monomeric versus fibrillar state.

a – 5 µL is the minimal working volume for sample injection, < 250 nl of sample is used for the analysis; b – based on the method used here which includes washing steps; c – asymmetric peak = not diffusive or slowly diffusive aggregates; spikes = large, non-diffusive aggregates; absence of spikes and asymmetric peak = large and macroscopic aggregates that do not enter the capillary; d – removal of most aggregates by centrifugation followed by FIDA allows more reliable sizing of the residual soluble species; e – using Type 42.2 Ti Fixed-Angle Titanium Rotor (Beckman); f – e.g. pipetting in and out of the centrifugation tubes and absorbance measurement off-line; g – using 384-well plates and 30 min read time/plate; h –ThT signal is not always linearly dependent on fibril concentration; i – using DSF capillary-based platforms such as Prometheus Panta (NanoTemper).

FIDA – Flow-induced dispersion analysis, UCF – ultracentrifugation, ThT – Thioflavin T assay, SLS – static light scattering, DLS – dynamic light scattering, DSF – Differential scanning fluorimetry. HTP – high-throughput,

Thermodynamic stability of aSyn fibrils is a valuable probe of fibril polymorphism.

Multiple polymorphs of αSyn fibrils have been observed in both patient samples [61-62] and *in vitro* studies using recombinant monomer [63-64]. The structural variation of fibrils assembled *in vitro* is dictated by the solution conditions of the aggregation assay, including pH, salt concentration, incubation temperature, or shaking [63-64]. Conversely, the diversity of fibril polymorphs isolated *ex vivo* may be attributed to the unique cellular environments [65] characteristic for each disease (similarly to what has been observed for the tau protein [9]). These include dopaminergic neurons in PD and oligodendrocytic glial cells in different brain regions in MSA [61, 66]. This is supported by the finding of unknown electron densities in the structures of both disease-related αSyn polymorphs, indicating a cell specific "aggregation co-factor" whose absence explains the inability to replicate these structures *in vitro* using seeded experiments [11]. While it is plausible for different fibril polymorphs to nucleate in a cellular environment, disease-specific polymorph evidence suggests that only one polymorph emerges as the dominant competitor, propagating itself due to higher stability, faster kinetics, or better compatibility with the cellular environment, including ligands or post-translational modifications (PTMs).

We studied the effect of salt and pH separately on the thermodynamic stability of the fibrils. We first prepared the fibrils in the absence or presence of salt (150 mM KCl) as well as neutral (pH 7.4) and acidic (pH 5) conditions. It has been reported that a distinct dominant polymorph is formed in each

condition [53, 67] which is supported by the morphological differences observed in our AFM analysis of the fibrils (Figure 4 c).

The thermodynamic stability of the polymorph S (salt condition) and NS (non-salt) was similar when assayed in the conditions at which they were formed (**Figure 5a**). However, the polymorph NS was more stable than polymorph S when measured in the buffer conditions in which the latter was formed (Figure 5a). The result was unexpected since the kinetics of fibril formation was faster at high salt, both in terms of nucleation and elongation (**SI figure 5)**. In contrast, the aggregation of αSyn in the absence of salt was slow and the reaction had to be promoted by sonication during the time course of reaction to achieve complete conversion of monomers to fibrils. Analysis of the aggregation kinetics in the presence of preformed seeds revealed that elongation saturates already at low μM concentrations of monomer, which might explain the need for sonication which promotes formation of new elongation-competent fibril ends and greatly accelerates the overall conversion of monomer to fibrils (**Error! Reference source not found.** b, right panel). To rationalize all our observations, we consider that αSyn can adopt different conformations during fibril formation [63-64]. High ionic strength increases the screening of charge repulsion between monomers and fibrils [68]. Consequently, the fibril conformations with lowest energy barrier of nucleation/elongation are formed first, i.e., the structural polymorphism is dominated by kinetic factors. This might lead to structures that are not optimised to avoid electrostatic repulsion, because such avoidance is not necessary under highly screened conditions. In contrast, the high electrostatic repulsion in the absence of salt creates an energy barrier leading to slower aggregation. In this scenario, the formation of amyloid fibrils is driven by αSyn conformations with an optimally minimized set of unfavourable electrostatic interactions and maximization of favourable interactions to ensure fibril stability under such unfavourable conditions. In other words, structural polymorphism is primarily influenced by thermodynamic stability of the resulting fibrils. These polymorphs exhibit enhanced stability compared to the kinetically controlled ones when transferred to the conditions where electrostatic forces are attenuated (high salt). The NS polymorph represents a low and possibly the global energy minimum on the rugged conformational landscape for neutral pH conditions which is unlikely to be sampled in the physiologically relevant context due to the easier accessibility of other fibril morphologies at physiological ionic strength. However, it provides important insights into the delicate interplay between kinetic and thermodynamic factors and their influence on fibril stability and polymorphism.

Changes in fibril stability in response to pH variation are likely to have more physiological relevance. It has been reported that fibrils formed in under conditions that simulate the acidic cellular compartments (lysosomes, endosomes) are destabilized when transferred to the neutral pH of the cytosolic environment [55]. Our results agree with such observations and provide a quantitative view of this phenomenon. Aggregation of αSyn under acidic pH conditions is faster and the resulting fibrils (H) are slightly more stable compared to a neutral pH (Figure 4b, Figure 5b; SI figure 5 c and d). In contrast

to the case above, the solubility differs between the fibril-forming conditions which explains the higher stability of fibrils at pH 5. However, the stability of H fibrils decreases upon transfer to physiological pH even below the stability of fibrils formed under such conditions. This indicates that a given fibril structure can be well-adapted to a given set of solution conditions, while a change in solution conditions can severely destabilize the structure. A change in pH can lead to a significant change in charge state of a protein and hence can lead to the emergence of additional unfavourable electrostatic interactions that render the given structure ill-adapted to the new solution environment.

To conclude, we demonstrate the importance of thermodynamic stability measurements in probing the rugged amyloid landscape and provide useful novel methodology for its analysis. We believe that future studies, that link thermodynamic stability of fibril polymorphs with high resolution structural information can provide a missing link between the observed structural polymorphism of amyloid fibrils and the properties relevant for disease.

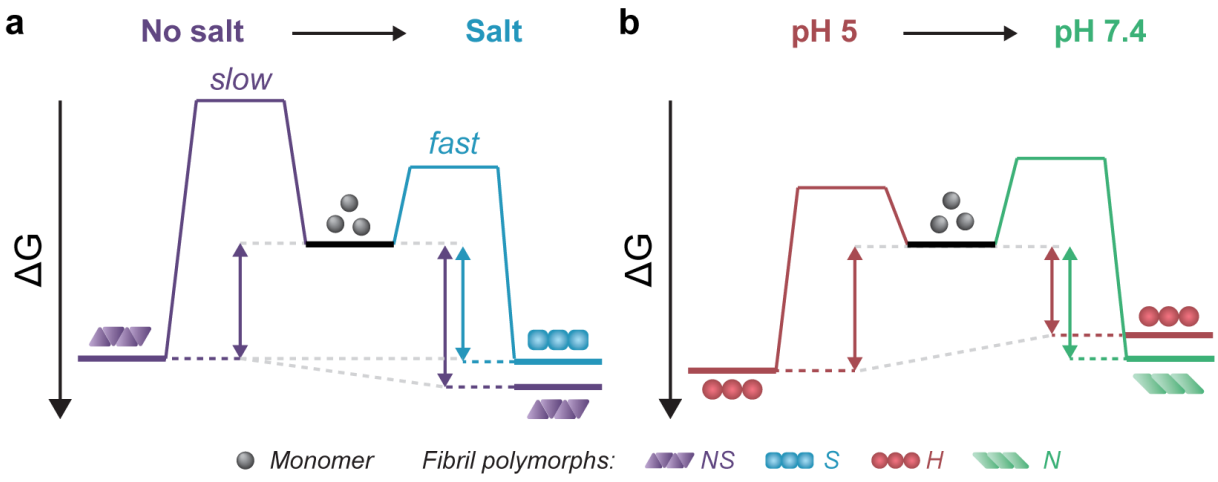

Figure 5. Schematic representation of energy landscapes of the different types of αSyn fibrils studied. Effect of (a) salt and (b) pH on kinetics and stability of fibrils. A change in solution conditions can both increase (a) and decrease (b) the thermodynamic stability of a given type of fibril.

Materials and Methods

Protein purification and sample preparation

Human wild type or F94W mutant αSyn were expressed in *E. coli* BL21 (DE3) cells transformed by the pT7-7 plasmid carrying the respective gene (Addgene plasmid # 36046; http://n2t.net/addgene:36046; RRID: Addgene_36046 [69]). Transformed cells were used to inoculate 1 L LB media containing ampicillin (50 µg/ml final concentration) as a selection marker. Cell suspension was incubated at 37 °C and αSyn expression induced by IPTG (1 mM final concentration) at OD_{600}

~0.6-0.8. The cells were harvested by centrifugation (5,000 x g, 20 minutes) following the 4-hour expression at 37 °C. Cell pellet corresponding to 1 L culture was resuspended in 20 mL of Tris buffer (10 mM Tris-HCl, 1 mM EDTA, pH 8.0) with 1 mM PMSF (phenylmethylsulfonyl fluoride). The suspension was sonicated with a probe ultrasonicator for 8 min (10 s on time, 30 s off time, 12 rounds with 40 % amplitude). 1 µL Benzonase (DNAase) was added to the cell lysate and the insoluble fraction was removed by centrifugation (20,000 × g, 30 min at 4 °C). The resulting cell-free extract was boiled for 20 min and the heat-precipitated proteins removed by centrifugation (20,000 × g for 20 min at 4 °C). αSyn was precipitated by addition of saturated $(NH_4)_2SO_4$ (4 mL per 1 mL of supernatant). The solution was incubated on a rocking platform at 4 °C for 15 min and then centrifuged (20,000 × g, 20 min, 4°C) to obtain a protein pellet. The pellet was dissolved in 7 mL of 25 mM Tris-HCl pH 7.7 with 1 mM DTT. Protein was dialyzed against the same buffer for 16–18 h with a buffer exchange after 12 h of dialysis at 4 °C. The dialyzed protein was then subjected to anion exchange chromatography (AEC) (HiTrap Q Hp 5 ml, GE healthcare) followed by size exclusion chromatography (SEC) (HiLoad 16/600 Superdex 200 pg. column). Monomeric fraction of αSyn eluted in 10 mM of sodium phosphate buffer (pH 7.4) was collected, and protein concentration determined by UV-absorption at 280 with theoretical molar extinction coefficients calculated from the protein sequence using ProtParam80 (Expasy, Switzerland).

Fibril preparation

The αSyn fibrils were prepared using a single monomer batch which was transferred to different buffer conditions (200 µM final monomer concentration) followed by incubation in the benchtop thermo-shaker with constant agitation (1,200 rpm) at 37 °C for 7 days. Fibril samples were frozen and stored at -20 °C. Prior to the experiment, fibrils were thawed and sonicated using probe ultrasonic (Heilscher *UP200St*). Sonication was carried out in repeating intervals of 3-second pulse with 20 % amplitude and 12-second pause for 5 minutes (one minute total sonication time) to prevent sample overheating.

Flow-induced dispersion analysis of non-diffusive particles

The flow-induced dispersion analysis (FIDA) experiments were carried out using FIDA1 instrument (FidaBio, Denmark). For each measurement, the following method was used unless stated otherwise:

1- Wash 1 (1M NaOH): 45 s, 3500 mbar.
2- Wash 2 (MQ water): 45 s, 3500 mbar.
3- Equilibration (Buffer): 30 s, 3500 mbar.
4- Sample application (Protein/NP stock): 20 s, 75 mbar.
5- Measurement and detection (Buffer): 75 s, 1500 mbar.

All FIDA experiments were performed at 25°C. The resulting Taylorgrams were corrected for the viscosity of urea according to the following empirical formula derived in [70]:

Eq. 5. $$\frac{\eta}{\eta 0} = 1 + 3.75 \times 10^{-2}.(C) + 3.15 \times 10^{-3}.(C)^2 + 3.10 \times 10^{-4}.(C)^3$$

where η is the viscosity of the sample, C is concentration of urea (in moles per liter), and η_0 is the viscosity of water.

The monomer quantification was carried out using four different methods of Taylorgram deconvolution following the reasoning that (i) the observed signal is a sum of contributions from diffusive particles (i.e., monomers) with a Gaussian distribution, and non-diffusive particles (i.e., fibrils/nanoparticles) exhibiting an asymmetrical distribution, and (ii) that the monomer concentration is proportional to the signal amplitude of the former.

Method 1: Baseline subtraction

The contribution from the non-diffusive particles was subtracted from the monomer signal using linear baseline connecting manually selected points at the intersects of the two distributions using OriginPro (OriginLab, USA). The monomer concentration was determined from the integral of the resulting peak.

Method 2: Independent fitting

Each Taylorgram was fitted to the sum of the Gaussian and asymmetrical distributions (Asym2Sig; OriginPro 2021) described by the Equations 6 and 7, respectively.

Eq. 6. $$y = y_0 + A_1/\left(w\sqrt{\pi/2}\right) exp(-2(t - t_{r1})^2/w^2)$$

Where y_0 is the signal offset, and t_r, A, and *w* are the peak centre (retention time, i.e., time for average flow to reach the detector), area, and width (reflecting the size of the monomers), respectively.

Eq. 7. $$y = \left[A_2/\left(1 + exp(-(t - t_{r2} + w_1/2)/w_2)\right)\right]\left[1 - 1/\left(1 + exp(-(t - t_{r2} - w_1/2)/w_3)\right)\right]$$

Here, w_1 denotes the full width of half maximum, and parameters w_2 and w_3 represent the variance of the left- and right-sides of the peak, respectively. Consequently, a symmetrical distribution is recovered when $w_2 = w_3$. The retention times of the two distributions were fixed together with the width of the Gaussian peak and the offset to reduce the number of parameters during fitting. The monomer concentration was determined from the area of the Gaussian peak.

Method 3: Global fitting

Fits of individual Taylorgrams often suffered from overparameterization and did not converge, most notably in cases where the contribution from the non-diffusive particles to the overall signal was low (0 - 10%). To overcome this, Taylorgrams across the whole urea depolymerization series were analyzed globally.

A global fit allows shared parameters across all data obtained for one series of measurements at different denaturant concentrations, which restricts the model and makes fitting more robust. The residency time (retention time) of the samples should be independent of urea after normalizing the data based the viscosity increase and was therefore shared between all samples. The hydrodynamic radius of the monomer was shown to be independent of denaturant and could thus be represented with Gauss curves with shared widths (Eq. 6) but different total areas which were defined by the isodesmic polymerization model (Eq. 8, [38]) multiplied with a constant to relate fluorescence to concentration.

Eq. 8.
$$y = \frac{2[M]_{tot}.\exp\left(-\frac{\Delta G+m.[D]}{RT}\right)+1-\sqrt{2[M]_{tot}.\exp\left(-\frac{\Delta G+m.[D]}{RT}\right)}}{2{[M]_{tot}}^{2}.\exp\left(-\frac{\Delta G+m.[D]}{RT}\right)^{2}}$$

Where $[M]_{tot}$ is the total concentration of the protein, *m* (or *m* value) is the denaturant dependency, [*D*] is the concentration of the denaturant, *R* is gas constant, and *T* is temperature.

We found that the signal for the fibrils changed slightly with urea, however this change could not be directly modelled by the empirical fit using the asymmetric distribution (Eq. 7). Also, the amount of fibrils present in the signal was stochastically changing in each sample due to sticking, sampling-issues due to heterogeneous samples and sedimentation, etc. To limit the over-parameterization and correlation between parameters in the fit, which made the estimation of monomer unreliable, the global analysis therefore used a shared asymmetric distribution curve to account for the fibril signal in all samples, and only the total area of the fibril signal was an independent fit parameter for each individual measurement. Because clumping fibrils caused spikes in the signal, all samples were smoothed using a median filter with a window size of 31 data points. Least squares fit was performed with lmfit in Python using the Levenberg-Marquardt algorithm (the code is available online).

Method 4: COMSOL simulation

Monomer and fibril transport were simulated using COMSOL Multiphysics 5.6 (COMSOL AB, Sweden) finite element analysis software. The simulated geometry was a straight capillary 1m in length aligned along the z-axis with a cylindrical 500 µm detector region at z = 840 mm.

Using the “Transport of Diluted Species” interface, a Poiseuille velocity field was imposed in the channel, with the magnitude determined by a parameterized pressure/viscosity term that was variable in time. In the first 20 seconds of the simulation, the velocity corresponded to an inlet pressure of 75 mbar, and two solute species were introduced by concentration constraint at the inlet, resulting in the introduction of a sample "plug". After 20 seconds, the concentration constraint at the inlet was set to zero and the pressure parameter increased to a value corresponding to the desired experimental velocity. The concentration of each species at the detector was recorded as a function of simulation time.

The simulation output was calibrated against experimental data from monomer-only runs. As the total protein concentration was constant (20 μM), and only the leading edge of the peak was used as reference data (avoiding confounding effects from adsorption of fibrils to the capillary walls), a separate calibration factor for fibrils was computed. The hydrodynamic radius of the monomer was experimentally determined using the FIDA 1 instrument, and its diffusion coefficient used as derived (7.0 e^{-11} m^2/s). An approximate fibril diffusion coefficient (D_f) was derived from a COMSOL fit to an experimental FIDA run for fibrils and confirmed by calculation of approximate expected values for fibrils of the experimentally determined average length (1.2 e^{-11} m^2/s).

Using the "Parameter Estimation interface", the free monomer concentration, fibril diffusion coefficient and fibril concentration/signal calibration multiplier were used as fitting parameters with the first 30 seconds of each experimental run as reference data. The fibril signal calibration value was entered as a fitting parameter to verify consistency of results.

DSF and static light scattering (SLS)

Intrinsic fluorescence and light scattering of the fibrils equilibrated at different concentrations of urea were measured using the Prometheus Panta instrument (NanoTemper, Germany). Samples were loaded into the standard grade capillaries and their fluorescence and light scattering recorded for 30 min at 25 °C. Scattering intensity was averaged over the measured timespan and normalized based on the assumption that fibrils at the lowest (0) and the highest concentration of urea (5.4 M) contain negligible amounts of free monomer or are completely dissociated, respectively.

Thioflavin T (ThT) fluorescence

In the ThT experiments, 10 μM ThT was added to the equilibrated samples (3 days, 25 °C), and their fluorescence (ex./em. = 440/480 nm) was recorded in a 384-well plate (Corning® 384-well Black and Clear Bottom; Corning 3544) using Omega Fluorescence plate reader (BMG Labtech, Germany).

Aggregation kinetics

Aggregation kinetics of wt αSyn were monitored under seeded and non-seeded conditions by ThT assay (ex./em. = 440/480 nm, 50 μM ThT). In the seeded experiments, 2.5 μM of sonicated seeds pre-formed at the same conditions as the respective experiment were added to the varying concentrations of fresh monomeric αSyn. The elongation kinetics were measured in the 384-well low volume non-binding black plates with clear bottom (Corning 3544) under quiescent conditions at 37 °C. Quantification of the residual monomer at the end of the aggregation reaction was carried out for samples with the highest initial monomer concentration by FIDA and used to convert the ThT signal into concentration of the fibrils (in monomer equivalents). The apparent elongation rates were obtained from slopes of the linear curves fitted into the initial timepoints (5 hours).

In the non-seeded experiments, varying concentrations of monomeric WT αSyn in different buffer conditions were incubated with a single glass bead (d = 1 mm) in the 384-well low volume non-treated polystyrene plates (Corning 3540) at 37 °C and the ThT fluorescence was monitored during continuous shaking (300 rpm, double orbital). Resulting datasets were fitted individually to a logistic function described by the equation 9.

Eq. 9.: $$y = y_0 + A/\left(1 + exp\left(-k(t - t_{0.5})\right)\right)$$

The y_0 is the pre-transition baseline, A is the signal amplitude, k is the apparent growth rate, and $t_{0.5}$ is the midpoint of the transition, i.e., half-time [71].

Ultracentrifugation

Fibril samples equilibrated in 72 hours at different concentrations of urea were ultracentrifuged (180,000 x g, 1 h, 25 °C) to pellet the aggregated fraction. The supernatant was carefully collected to an Eppendorf tube and the concentration of the residual monomer determined by UV absorption using a NanoDrop instrument (ThermoFisher, USA) and the extinction coefficients of the respective variants (WT or F94W).

AFM imaging and analysis of the fibrils

Fibrils were diluted to 5 µM monomer equivalent concentration and 10 µL of the solution was pipetted onto freshly cleaved mica substrates. Following 10 min of incubation, the substrates were cleaned extensively with miliQ water and dried under air flow. All fibrils were imaged in tapping mode in air using a DriveAFM (Nanosurf, Liestal, Switzerland) using PPP-NCLAuD cantilevers (Nanosensors, Neuchatel, Switzerland).

Amyloid fibrils are characterized by pitch length and height. Fibril pitch is analyzed from fibril height profiles along the fibril length extracted using Gwyddion. Multiple pixel averages have been used to measure slightly curved fibrils. This is acceptable for analysis since the absolute height of the fibrils does not influence pitch analysis. Additionally, length profiles shorter than 300 nm are excluded from the analysis. The Fourier transforms of the fibril height profiles were computed, using the *fft* and *fftfreq* modules of the *scipy.fft* python library. To avoid the frequency domain being dominated by measurement noise and the mean fibril profile, frequencies translating to length scales below 5 pixel-lengths and above 1/3 of the full fibril or profile length are excluded. From the remaining frequency domain, the primary frequency peak is identified as the frequency of fibril rotation and converted to length to obtain the periodicity. The pitch length (full 360 degree rotation) is calculated as double the length of a single fibril rotation. Fibril height is analyzed from fibril cross-section profiles extracted using Gwyddion. The surface baseline is calculated as the median height of the cross-section and fibril height is calculated from the peak of the cross-section.

References:

1. Chiti, F.; Dobson, C. M., Protein Misfolding, Amyloid Formation, and Human Disease: A Summary of Progress Over the Last Decade. *Annu Rev Biochem* **2017,** *86*, 27-68.
2. Louros, N.; Konstantoulea, K.; De Vleeschouwer, M.; Ramakers, M.; Schymkowitz, J.; Rousseau, F., WALTZ-DB 2.0: an updated database containing structural information of experimentally determined amyloid-forming peptides. *Nucleic Acids Res* **2020,** *48* (D1), D389-D393.
3. Mehra, S.; Gadhe, L.; Bera, R.; Sawner, A. S.; Maji, S. K., Structural and Functional Insights into alpha-Synuclein Fibril Polymorphism. *Biomolecules* **2021,** *11* (10).
4. Sunde, M.; Serpell, L. C.; Bartlam, M.; Fraser, P. E.; Pepys, M. B.; Blake, C. C., Common core structure of amyloid fibrils by synchrotron X-ray diffraction. *J Mol Biol* **1997,** *273* (3), 729-39.
5. Iadanza, M. G.; Silvers, R.; Boardman, J.; Smith, H. I.; Karamanos, T. K.; Debelouchina, G. T.; Su, Y.; Griffin, R. G.; Ranson, N. A.; Radford, S. E., The structure of a beta(2)-microglobulin fibril suggests a molecular basis for its amyloid polymorphism. *Nat Commun* **2018,** *9* (1), 4517.
6. Roder, C.; Vettore, N.; Mangels, L. N.; Gremer, L.; Ravelli, R. B. G.; Willbold, D.; Hoyer, W.; Buell, A. K.; Schroder, G. F., Atomic structure of PI3-kinase SH3 amyloid fibrils by cryo-electron microscopy. *Nat Commun* **2019,** *10* (1), 3754.
7. Hoppenreijs, L. J. G.; Fitzner, L.; Ruhmlieb, T.; Heyn, T. R.; Schild, K.; van der Goot, A. J.; Boom, R. M.; Steffen-Heins, A.; Schwarz, K.; Keppler, J. K., Engineering amyloid and amyloid-like morphologies of β-lactoglobulin. *Food Hydrocolloids* **2022,** *124*.
8. Gazit, E., The "Correctly Folded" state of proteins: is it a metastable state? *Angew Chem Int Ed Engl* **2002,** *41* (2), 257-9.
9. Shi, Y.; Zhang, W.; Yang, Y.; Murzin, A. G.; Falcon, B.; Kotecha, A.; van Beers, M.; Tarutani, A.; Kametani, F.; Garringer, H. J.; Vidal, R.; Hallinan, G. I.; Lashley, T.; Saito, Y.; Murayama, S.; Yoshida, M.; Tanaka, H.; Kakita, A.; Ikeuchi, T.; Robinson, A. C.; Mann, D. M. A.; Kovacs, G. G.; Revesz, T.; Ghetti, B.; Hasegawa, M.; Goedert, M.; Scheres, S. H. W., Structure-based classification of tauopathies. *Nature* **2021,** *598* (7880), 359-363.
10. Ghosh, U.; Thurber, K. R.; Yau, W. M.; Tycko, R., Molecular structure of a prevalent amyloid-beta fibril polymorph from Alzheimer's disease brain tissue. *Proc Natl Acad Sci U S A* **2021,** *118* (4).
11. Lovestam, S.; Schweighauser, M.; Matsubara, T.; Murayama, S.; Tomita, T.; Ando, T.; Hasegawa, K.; Yoshida, M.; Tarutani, A.; Hasegawa, M.; Goedert, M.; Scheres, S. H. W., Seeded assembly in vitro does not replicate the structures of alpha-synuclein filaments from multiple system atrophy. *FEBS Open Bio* **2021,** *11* (4), 999-1013.
12. Ziaunys, M.; Sakalauskas, A.; Mikalauskaite, K.; Smirnovas, V., Polymorphism of Alpha-Synuclein Amyloid Fibrils Depends on Ionic Strength and Protein Concentration. *Int J Mol Sci* **2021,** *22* (22).
13. Knowles, T. P.; Waudby, C. A.; Devlin, G. L.; Cohen, S. I.; Aguzzi, A.; Vendruscolo, M.; Terentjev, E. M.; Welland, M. E.; Dobson, C. M., An analytical solution to the kinetics of breakable filament assembly. *Science* **2009,** *326* (5959), 1533-7.
14. Meisl, G.; Kirkegaard, J. B.; Arosio, P.; Michaels, T. C.; Vendruscolo, M.; Dobson, C. M.; Linse, S.; Knowles, T. P., Molecular mechanisms of protein aggregation from global fitting of kinetic models. *Nat Protoc* **2016,** *11* (2), 252-72.
15. Michaels, T. C. T.; Saric, A.; Habchi, J.; Chia, S.; Meisl, G.; Vendruscolo, M.; Dobson, C. M.; Knowles, T. P. J., Chemical Kinetics for Bridging Molecular Mechanisms and Macroscopic Measurements of Amyloid Fibril Formation. *Annu Rev Phys Chem* **2018,** *69*, 273-298.
16. Cohen, S. I.; Linse, S.; Luheshi, L. M.; Hellstrand, E.; White, D. A.; Rajah, L.; Otzen, D. E.; Vendruscolo, M.; Dobson, C. M.; Knowles, T. P., Proliferation of amyloid-beta42 aggregates occurs through a secondary nucleation mechanism. *Proc Natl Acad Sci U S A* **2013,** *110* (24), 9758-63.
17. Kundel, F.; Hong, L.; Falcon, B.; McEwan, W. A.; Michaels, T. C. T.; Meisl, G.; Esteras, N.; Abramov, A. Y.; Knowles, T. J. P.; Goedert, M.; Klenerman, D., Measurement of Tau Filament

680 Fragmentation Provides Insights into Prion-like Spreading. *ACS Chem Neurosci* **2018,** *9* (6), 1276-
681 1282.
682 18. Galvagnion, C.; Buell, A. K.; Meisl, G.; Michaels, T. C.; Vendruscolo, M.; Knowles, T. P.;
683 Dobson, C. M., Lipid vesicles trigger alpha-synuclein aggregation by stimulating primary nucleation.
684 *Nat Chem Biol* **2015,** *11* (3), 229-34.
685 19. Buell, A. K.; Galvagnion, C.; Gaspar, R.; Sparr, E.; Vendruscolo, M.; Knowles, T. P.; Linse,
686 S.; Dobson, C. M., Solution conditions determine the relative importance of nucleation and growth
687 processes in alpha-synuclein aggregation. *Proc Natl Acad Sci U S A* **2014,** *111* (21), 7671-6.
688 20. Buell, A. K., Stability matters, too - the thermodynamics of amyloid fibril formation.
689 *Chem Sci* **2022,** *13* (35), 10177-10192.
690 21. Donzelli, S.; Osullivan, S. A.; Mahul-Mellier, A.-L.; Ulusoy, A.; Fusco, G.; Kumar, S. T.;
691 Chiki, A.; Burtscher, J.; Boussouf, M. L. D.; Rostami, I.; Simone, A. D.; Di Monte, D. A.; Lashuel, H. A.,
692 Post-fibrillization nitration of alpha-synuclein abolishes its seeding activity and pathology formation
693 in primary neurons and in vivo. *BioRxiv* **2023**.
694 22. Altay, M. F.; Liu, A. K. L.; Holton, J. L.; Parkkinen, L.; Lashuel, H. A., Prominent astrocytic
695 alpha-synuclein pathology with unique post-translational modification signatures unveiled across
696 Lewy body disorders. *Acta Neuropathol Commun* **2022,** *10* (1), 163.
697 23. Cliffe, R.; Sang, J. C.; Kundel, F.; Finley, D.; Klenerman, D.; Ye, Y., Filamentous
698 Aggregates Are Fragmented by the Proteasome Holoenzyme. *Cell Rep* **2019,** *26* (8), 2140-2149 e3.
699 24. Wentink, A.; Nussbaum-Krammer, C.; Bukau, B., Modulation of Amyloid States by
700 Molecular Chaperones. *Cold Spring Harb Perspect Biol* **2019,** *11* (7).
701 25. Franco, A.; Gracia, P.; Colom, A.; Camino, J. D.; Fernandez-Higuero, J. A.; Orozco, N.;
702 Dulebo, A.; Saiz, L.; Cremades, N.; Vilar, J. M. G.; Prado, A.; Muga, A., All-or-none amyloid disassembly
703 via chaperone-triggered fibril unzipping favors clearance of alpha-synuclein toxic species. *Proc Natl*
704 *Acad Sci U S A* **2021,** *118* (36).
705 26. Almeida, Z. L.; Brito, R. M. M., Amyloid Disassembly: What Can We Learn from
706 Chaperones? *Biomedicines* **2022,** *10* (12).
707 27. Hellstrand, E.; Boland, B.; Walsh, D. M.; Linse, S., Amyloid beta-protein aggregation
708 produces highly reproducible kinetic data and occurs by a two-phase process. *ACS Chem Neurosci*
709 **2010,** *1* (1), 13-8.
710 28. Sawaya, M. R.; Hughes, M. P.; Rodriguez, J. A.; Riek, R.; Eisenberg, D. S., The expanding
711 amyloid family: Structure, stability, function, and pathogenesis. *Cell* **2021,** *184* (19), 4857-4873.
712 29. Kardos, J.; Yamamoto, K.; Hasegawa, K.; Naiki, H.; Goto, Y., Direct measurement of the
713 thermodynamic parameters of amyloid formation by isothermal titration calorimetry. *J Biol Chem*
714 **2004,** *279* (53), 55308-14.
715 30. Morel, B.; Varela, L.; Conejero-Lara, F., The thermodynamic stability of amyloid fibrils
716 studied by differential scanning calorimetry. *J Phys Chem B* **2010,** *114* (11), 4010-9.
717 31. Ikenoue, T.; Lee, Y. H.; Kardos, J.; Saiki, M.; Yagi, H.; Kawata, Y.; Goto, Y., Cold
718 denaturation of alpha-synuclein amyloid fibrils. *Angew Chem Int Ed Engl* **2014,** *53* (30), 7799-804.
719 32. Norrild, R. K.; Vettore, N.; Coden, A.; Xue, W. F.; Buell, A. K., Thermodynamics of
720 amyloid fibril formation from non-equilibrium experiments of growth and dissociation. *Biophys Chem*
721 **2021,** *271*, 106549.
722 33. van Gils, J. H. M.; van Dijk, E.; Peduzzo, A.; Hofmann, A.; Vettore, N.; Schutzmann, M.
723 P.; Groth, G.; Mouhib, H.; Otzen, D. E.; Buell, A. K.; Abeln, S., The hydrophobic effect characterises the
724 thermodynamic signature of amyloid fibril growth. *PLoS Comput Biol* **2020,** *16* (5), e1007767.
725 34. Meersman, F.; Dobson, C. M., Probing the pressure-temperature stability of amyloid
726 fibrils provides new insights into their molecular properties. *Biochim Biophys Acta* **2006,** *1764* (3),
727 452-60.
728 35. Narimoto, T.; Sakurai, K.; Okamoto, A.; Chatani, E.; Hoshino, M.; Hasegawa, K.; Naiki,
729 H.; Goto, Y., Conformational stability of amyloid fibrils of beta2-microglobulin probed by guanidine-
730 hydrochloride-induced unfolding. *FEBS Lett* **2004,** *576* (3), 313-9.

731 36. Raimondi, S.; Mangione, P. P.; Verona, G.; Canetti, D.; Nocerino, P.; Marchese, L.;
732 Piccarducci, R.; Mondani, V.; Faravelli, G.; Taylor, G. W.; Gillmore, J. D.; Corazza, A.; Pepys, M. B.;
733 Giorgetti, S.; Bellotti, V., Comparative study of the stabilities of synthetic in vitro and natural ex vivo
734 transthyretin amyloid fibrils. *J Biol Chem* **2020,** *295* (33), 11379-11387.
735 37. Sulatsky, M. I.; Sulatskaya, A. I.; Stepanenko, O. V.; Povarova, O. I.; Kuznetsova, I. M.;
736 Turoverov, K. K., Denaturant effect on amyloid fibrils: Declasterization, depolymerization,
737 denaturation and reassembly. *Int J Biol Macromol* **2020,** *150*, 681-694.
738 38. Vettore, N.; Buell, A. K., Thermodynamics of amyloid fibril formation from chemical
739 depolymerization. *Physical chemistry chemical physics : PCCP* **2019,** *21* (47), 26184-26194.
740 39. Santoro, M. M.; Bolen, D. W., Unfolding free energy changes determined by the linear
741 extrapolation method. 1. Unfolding of phenylmethanesulfonyl alpha-chymotrypsin using different
742 denaturants. *Biochemistry* **1988,** *27* (21), 8063-8.
743 40. Smulders, M. M.; Nieuwenhuizen, M. M.; de Greef, T. F.; van der Schoot, P.; Schenning,
744 A. P.; Meijer, E. W., How to distinguish isodesmic from cooperative supramolecular polymerisation.
745 *Chemistry* **2010,** *16* (1), 362-7.
746 41. Baldwin, A. J.; Knowles, T. P.; Tartaglia, G. G.; Fitzpatrick, A. W.; Devlin, G. L.; Shammas,
747 S. L.; Waudby, C. A.; Mossuto, M. F.; Meehan, S.; Gras, S. L.; Christodoulou, J.; Anthony-Cahill, S. J.;
748 Barker, P. D.; Vendruscolo, M.; Dobson, C. M., Metastability of native proteins and the phenomenon
749 of amyloid formation. *J Am Chem Soc* **2011,** *133* (36), 14160-3.
750 42. Taylor, G. I., Dispersion of soluble matter in solvent flowing slowly through a tube.
751 *Proceedings of the Royal Society of London. Series A. Mathematical and Physical Sciences* **1953,** *219*
752 (1137), 186-203.
753 43. Pedersen, M. E.; Ostergaard, J.; Jensen, H., Flow-Induced Dispersion Analysis (FIDA) for
754 Protein Quantification and Characterization. *Methods Mol Biol* **2019,** *1972*, 109-123.
755 44. Jensen, H.; Ostergaard, J., Flow induced dispersion analysis quantifies noncovalent
756 interactions in nanoliter samples. *J Am Chem Soc* **2010,** *132* (12), 4070-1.
757 45. Rasmus Norrild , T. M., Lars Boyens-Thiele ,Soumik Ray ,Joachim Mortensen ,Anatol
758 Fritsch ,Juan Iglesias-Artola ,Louise Klausen ,Emil Stender ,Henrik Jensen ,Alexander Buell Taylor-
759 dispersion induced phase separation for the efficient characterisation of protein condensate
760 formation. *ChemRxiv.* **2023**.
761 46. Garcia de la Torre, J. G.; Bloomfield, V. A., Hydrodynamic properties of complex, rigid,
762 biological macromolecules: theory and applications. *Q Rev Biophys* **1981,** *14* (1), 81-139.
763 47. Royer, C. A., Probing protein folding and conformational transitions with fluorescence.
764 *Chem Rev* **2006,** *106* (5), 1769-84.
765 48. Protein Fluorescence. In *Principles of Fluorescence Spectroscopy*, Lakowicz, J. R., Ed.
766 Springer US: Boston, MA, 2006; pp 529-575.
767 49. Sidhu, A.; Vaneyck, J.; Blum, C.; Segers-Nolten, I.; Subramaniam, V., Polymorph-specific
768 distribution of binding sites determines thioflavin-T fluorescence intensity in alpha-synuclein fibrils.
769 *Amyloid* **2018,** *25* (3), 189-196.
770 50. Hudson, S. A.; Ecroyd, H.; Kee, T. W.; Carver, J. A., The thioflavin T fluorescence assay
771 for amyloid fibril detection can be biased by the presence of exogenous compounds. *FEBS J* **2009,**
772 *276* (20), 5960-72.
773 51. Ziaunys, M.; Sakalauskas, A.; Smirnovas, V., Identifying Insulin Fibril Conformational
774 Differences by Thioflavin-T Binding Characteristics. *Biomacromolecules* **2020,** *21* (12), 4989-4997.
775 52. Biancalana, M.; Koide, S., Molecular mechanism of Thioflavin-T binding to amyloid
776 fibrils. *Biochim Biophys Acta* **2010,** *1804* (7), 1405-12.
777 53. Bousset, L.; Pieri, L.; Ruiz-Arlandis, G.; Gath, J.; Jensen, P. H.; Habenstein, B.; Madiona,
778 K.; Olieric, V.; Bockmann, A.; Meier, B. H.; Melki, R., Structural and functional characterization of two
779 alpha-synuclein strains. *Nat Commun* **2013,** *4*, 2575.

54. Gath, J.; Bousset, L.; Habenstein, B.; Melki, R.; Bockmann, A.; Meier, B. H., Unlike twins: an NMR comparison of two alpha-synuclein polymorphs featuring different toxicity. *PLoS One* **2014,** *9* (3), e90659.
55. Eymsh, B.; Drobny, A.; Heyn, T. R.; Xiang, W.; Lucius, R.; Schwarz, K.; Keppler, J. K.; Zunke, F.; Arnold, P., Toxic Metamorphosis-How Changes from Lysosomal to Cytosolic pH Modify the Alpha-Synuclein Aggregation Pattern. *Biomacromolecules* **2020,** *21* (12), 4673-4684.
56. Streets, A. M.; Sourigues, Y.; Kopito, R. R.; Melki, R.; Quake, S. R., Simultaneous measurement of amyloid fibril formation by dynamic light scattering and fluorescence reveals complex aggregation kinetics. *PLoS One* **2013,** *8* (1), e54541.
57. Shen, C. L.; Scott, G. L.; Merchant, F.; Murphy, R. M., Light scattering analysis of fibril growth from the amino-terminal fragment beta(1-28) of beta-amyloid peptide. *Biophys J* **1993,** *65* (6), 2383-95.
58. De Giorgi, F.; Laferriere, F.; Zinghirino, F.; Faggiani, E.; Lends, A.; Bertoni, M.; Yu, X.; Grelard, A.; Morvan, E.; Habenstein, B.; Dutheil, N.; Doudnikoff, E.; Daniel, J.; Claverol, S.; Qin, C.; Loquet, A.; Bezard, E.; Ichas, F., Novel self-replicating alpha-synuclein polymorphs that escape ThT monitoring can spontaneously emerge and acutely spread in neurons. *Sci Adv* **2020,** *6* (40).
59. Uversky, V. N., The alphabet of intrinsic disorder: II. Various roles of glutamic acid in ordered and intrinsically disordered proteins. *Intrinsically Disord Proteins* **2013,** *1* (1), e24684.
60. Vacic, V.; Uversky, V. N.; Dunker, A. K.; Lonardi, S., Composition Profiler: a tool for discovery and visualization of amino acid composition differences. *BMC Bioinformatics* **2007,** *8*, 211.
61. Shahnawaz, M.; Mukherjee, A.; Pritzkow, S.; Mendez, N.; Rabadia, P.; Liu, X.; Hu, B.; Schmeichel, A.; Singer, W.; Wu, G.; Tsai, A. L.; Shirani, H.; Nilsson, K. P. R.; Low, P. A.; Soto, C., Discriminating alpha-synuclein strains in Parkinson's disease and multiple system atrophy. *Nature* **2020,** *578* (7794), 273-277.
62. Strohaker, T.; Jung, B. C.; Liou, S. H.; Fernandez, C. O.; Riedel, D.; Becker, S.; Halliday, G. M.; Bennati, M.; Kim, W. S.; Lee, S. J.; Zweckstetter, M., Structural heterogeneity of alpha-synuclein fibrils amplified from patient brain extracts. *Nat Commun* **2019,** *10* (1), 5535.
63. Hoyer, W.; Antony, T.; Cherny, D.; Heim, G.; Jovin, T. M.; Subramaniam, V., Dependence of alpha-synuclein aggregate morphology on solution conditions. *J Mol Biol* **2002,** *322* (2), 383-93.
64. Holec, S. A. M.; Liu, S. L.; Woerman, A. L., Consequences of variability in alpha-synuclein fibril structure on strain biology. *Acta Neuropathol* **2022,** *143* (3), 311-330.
65. Peng, C.; Gathagan, R. J.; Covell, D. J.; Medellin, C.; Stieber, A.; Robinson, J. L.; Zhang, B.; Pitkin, R. M.; Olufemi, M. F.; Luk, K. C.; Trojanowski, J. Q.; Lee, V. M., Cellular milieu imparts distinct pathological alpha-synuclein strains in alpha-synucleinopathies. *Nature* **2018,** *557* (7706), 558-563.
66. Schweighauser, M.; Shi, Y.; Tarutani, A.; Kametani, F.; Murzin, A. G.; Ghetti, B.; Matsubara, T.; Tomita, T.; Ando, T.; Hasegawa, K.; Murayama, S.; Yoshida, M.; Hasegawa, M.; Scheres, S. H. W.; Goedert, M., Structures of alpha-synuclein filaments from multiple system atrophy. *Nature* **2020,** *585* (7825), 464-469.
67. Peduzzo, A.; Linse, S.; Buell, A. K., The Properties of alpha-Synuclein Secondary Nuclei Are Dominated by the Solution Conditions Rather than the Seed Fibril Strain. *ACS Chem Neurosci* **2020,** *11* (6), 909-918.
68. Buell, A. K.; Hung, P.; Salvatella, X.; Welland, M. E.; Dobson, C. M.; Knowles, T. P., Electrostatic effects in filamentous protein aggregation. *Biophys J* **2013,** *104* (5), 1116-26.
69. Paleologou, K. E.; Schmid, A. W.; Rospigliosi, C. C.; Kim, H. Y.; Lamberto, G. R.; Fredenburg, R. A.; Lansbury, P. T., Jr.; Fernandez, C. O.; Eliezer, D.; Zweckstetter, M.; Lashuel, H. A., Phosphorylation at Ser-129 but not the phosphomimics S129E/D inhibits the fibrillation of alpha-synuclein. *J Biol Chem* **2008,** *283* (24), 16895-905.
70. Kawahara, K.; Tanford, C., Viscosity and density of aqueous solutions of urea and guanidine hydrochloride. *J Biol Chem* **1966,** *241* (13), 3228-32.

71. Arosio, P.; Knowles, T. P.; Linse, S., On the lag phase in amyloid fibril formation. *Physical chemistry chemical physics : PCCP* **2015,** *17* (12), 7606-18.